



E x B electron drift current across the aperture of an ion source surrounded by a cusped magnetic field profile

G. Fubiani, Yuchao Jiang, Jean-Pierre Boeuf

► To cite this version:

G. Fubiani, Yuchao Jiang, Jean-Pierre Boeuf. E x B electron drift current across the aperture of an ion source surrounded by a cusped magnetic field profile. *Physics of Plasmas*, 2020, 27 (9), pp.093506. 10.1063/5.0013639 . hal-02992345

HAL Id: hal-02992345

<https://hal.science/hal-02992345>

Submitted on 26 Nov 2020

HAL is a multi-disciplinary open access archive for the deposit and dissemination of scientific research documents, whether they are published or not. The documents may come from teaching and research institutions in France or abroad, or from public or private research centers.

L'archive ouverte pluridisciplinaire **HAL**, est destinée au dépôt et à la diffusion de documents scientifiques de niveau recherche, publiés ou non, émanant des établissements d'enseignement et de recherche français ou étrangers, des laboratoires publics ou privés.

$\mathbf{E} \times \mathbf{B}$ electron drift current across the aperture of an ion source surrounded by a cusped magnetic field profile

G. Fubiani,* Y. Jiang, and J. P. Boeuf

LAPLACE, Université de Toulouse, CNRS, 31062 Toulouse, France

Abstract

In negative ion sources, a cusped magnetic field is generated by magnets placed around each aperture of the extraction grid in order to limit the co-extracted electron current. In spite of this suppression magnetic field, the co-extracted electron current is large, on the same order as the negative ion current extracted from the plasma. In this paper we study the mechanisms of electron extraction from the plasma through a cusped aperture in a simplified situation, in the absence of negative ions, with the help of a three-dimensional Particle-In-Cell Monte Carlo Collisions (PIC-MCC) model. The calculation results show that the electron current extracted from the plasma is small for an infinite slit aperture with suppression (cusped) magnetic field and significantly increases in the case of finite slit or circular grid apertures. We find that $\mathbf{E} \times \mathbf{B}$ electron drift plays an important role in the extraction of electrons through a finite slit grid aperture and that current driven micro instabilities are present in the aperture region. This work is relevant to negative ion sources and micro-ECR neutralizers designed for space propulsion.

* gwenael.fubiani@laplace.univ-tlse.fr

I. INTRODUCTION

The question of electron extraction mechanisms from negative ion sources (and in particular of those used for fusion applications [1–6]) and in micro-ECR neutralizers for space propulsion [7, 8] is currently an open problem. In fusion type plasma sources, a magnetic cusp field (also called suppression field) is used to deflect extracted electrons onto the first grid of an electrostatic accelerator in order to prevent the acceleration to high energies of these particles. Electrons are co-extracted with negative ions (about the same current densities for both species). The acceleration voltage is 1 MV in the case of ITER and electrons can in principle damage the accelerator as a result of a high parasitic power density deposition on the accelerator grids [9, 10].

The magnetic field from the suppression magnets penetrates also inside the ion source plasma, a few centimetres in front of the plasma grid (PG). The latter has 1280 apertures in the case of ITER. We focus in this work specifically on the effect of the cusp magnetic field on the electron dynamics in that area (the cusp surrounds each apertures). The numerical model is hence simplified and we did not include negative ions. Their influence is briefly analysed in the discussion section. Furthermore, we do not simulate the whole ion source but rather a small area around the apertures. We also model exclusively slit apertures (the generalisation to circular geometry is straightforward). The plasma is generated artificially (a source term for the charged particles) on the left-hand-side (LHS) of the simulation domain. The first grid of the accelerator, which is commonly termed "extraction grid" (EG), is included in the calculation and is biased positively with respect to the PG. The bias voltage extracts an electron current from the plasma and induces the formation of a meniscus around each apertures. The meniscus separates the quasineutral plasma from the non-neutral region inside the accelerator. The cusp field amplitude decreases exponentially from the permanent magnet position, which is located in the model on the EG (same as in ITER and DEMO accelerator designs). Note that electrons are strongly magnetized while ions are somewhat magnetized but only over a short distance close to the aperture surface.

In the model, the cusp field is generated by two permanent magnet bars of reversed polarity parallel to the slit apertures. The magnetic vector field hence lies approximatively in the plane perpendicular to the magnets when the latter are much longer than the length of the aperture. We find that the electron flux diffusing across the aperture is driven by an

$\mathbf{E} \times \mathbf{B}$ drift where \mathbf{E} is the electric field in the vicinity of the plasma meniscus. The $\mathbf{E} \times \mathbf{B}$ drift occurs in the plane perpendicular to the cusp magnetic field lines. As a consequence, in an hypothetical configuration where a slit aperture is of infinite length, this $\mathbf{E} \times \mathbf{B}$ drift does not contribute to electron extraction. The flux of electrons through the aperture is much smaller in that case and is only due to collisional cross-field drift. We show that a 2D Particle-In-Cell (PIC) algorithm with Monte-Carlo-Collisions (MCC) is sufficient to capture the underlying physics of an infinite slit, and is consistent with results from a 3D PIC-MCC model. In the case of a finite slit, only a 3D model can describe properly electron extraction due to $\mathbf{E} \times \mathbf{B}$ drift through the aperture. Note that plasma electron extraction from a negative ion source has been previously studied analytically and with a ray-tracing approach in 1D and 2D by Cavenago et al. [11].

In the next section, we describe in details the simulation parameters. In sec. III, we analyse the mechanisms of electron extraction in the case of an infinite slit and for a finite slit aperture. In sec. IV, we describe some micro-instabilities occurring in the vicinity of the plasma meniscus in the case of a finite slit aperture. Lastly, sec. V and VI, provide a discussion and conclusions on the work presented in this paper.

II. OVERVIEW OF THE 2D AND 3D PIC-MCC MODELS

We developed 2D and 3D PIC-MCC electrostatic explicit models [12]. The electric field is calculated on the mesh nodes by solving Poisson's equation iteratively via a multi-grid algorithm [13]. The magnetic cusp field profile is derived from analytical considerations [14],

$$B_x = B_0 \sin \left[\frac{\pi (z - z_0)}{d} \right] \exp \left[-\frac{\pi (x_0 - x)}{d} \right] , \quad (1)$$

$$B_z = B_0 \cos \left[\frac{\pi (z - z_0)}{d} \right] \exp \left[-\frac{\pi (x_0 - x)}{d} \right] , \quad (2)$$

where B_0 is the maximum amplitude of the field, d is the distance between the magnet bars, x_0 is their axial coordinate and z_0 the center position between the two magnets, respectively. The norm of the magnetic field vector, $|\mathbf{B}|$, is decreasing exponentially from the location of the magnets. The particles trajectories are calculated by solving the Newton's equation of motion at the particle location (the electric and magnetic fields are interpolated),

$$m_p \frac{d\mathbf{v}_p}{dt} = q_p (\mathbf{E} + \mathbf{v}_p \times \mathbf{B}) , \quad (3)$$

where p either stands for electrons or ions, $\mathbf{E}(x, y, z)$ is the electrostatic field, $\mathbf{v}_p(t)$ the particle velocity and m_p (q_p) its mass (charge), respectively. The force on the RHS is the Lorentz force. In a PIC-MCC algorithm, charged particles are actually macro-particles but with the same charge over mass ratio as real electrons and ions. Once the particle positions have been updated, the density is calculated on the mesh nodes. This is used as a source term for Poisson's equations. In addition, we implemented collisions between charged particles and the neutral background gas using the Monte-Carlo technique [12, 15–17]. The PIC-MCC cycle described above is repeated iteratively. The collision processes are simplified in this problem. We considered only the elastic collisions between electrons and the positive ions or the neutrals (table I). The neutral background gas profile is assumed constant with a density of $n_n = 5 \times 10^{19} \text{ m}^{-3}$ and the gas temperature is set at $T_n = 0.1 \text{ eV}$. The average electron-neutral elastic collision frequency in the calculation is $\nu_{en} \simeq 5 \times 10^6 \text{ s}^{-1}$ (reaction #1 of table I) while the electron-ion collisions frequency is of order of $\nu_{ei} \simeq 1.2 \times 10^5 \text{ s}^{-1}$ (reaction #2), respectively. The average plasma density is $n_i = 5 \times 10^{15} \text{ m}^{-3}$ and the plasma generation is modelled by mimicking ionisation through the reinjection of an electron-positive ion pair for each positive ion lost on the physical boundaries of the simulation domain (i.e, of Dirichlet type). Note that the electron Debye length is typically about eight times larger than in the extraction region of negative ion source prototypes developed for ITER and DEMO [3, 18]. The particles are injected into the gray area shown schematically on the LHS of fig. 1 (dubbed "plasma source"). The electron distribution function is artificially maintained in that area as a Maxwellian at a temperature of $T_e = 2 \text{ eV}$ via the periodic replacement of the electron velocity (we use an artificial "heating" frequency). The positive ions are injected assuming also a Maxwellian distribution at a temperature $T_i = 2 \text{ eV}$ (although we do not enforce it in the plasma volume, only at the time when the ions are generated). The latter is the typical value for the average kinetic energy deduced from 3D PIC-MCC models of a fusion-type negative ion source [19]. We implemented a numerical resolution of $256 \times 384 \times 192$ grid nodes associated with a simulation box of physical dimensions $3.2 \times 4.8 \times 2.4 \text{ cm}^3$ (length versus width and height). The number of particles per cell is 40 and the time step $\omega_p \Delta t \simeq 0.2$. In addition, the size of the two slits is $4.3 \times 0.8 \text{ cm}^2$ (length times width) and the amplitude of the cusp magnetic field on the plasma grid (PG) is 200G, which corresponds to $B_0 = 875\text{G}$, $d = 1.2 \text{ cm}$, $x_0 = 3.2 \text{ cm}$, $z_0 = 0.6 \text{ cm}$ in eqs. (1) and (2), respectively. The cusped magnetic field profile encompasses each of the slit apertures, as shown on the

RHS of fig. 1. The direction of the magnetic field vector is reversed between neighbouring apertures. In addition, the numerical model is parallelized in an hybrid manner using the OpenMP and MPI libraries [12]. For the simulations reported in this paper, we typically used 48 OpenMP threads together with 4 MPI threads (one per node), i.e, 192 cores in total (on Intel Xeon CPU E5-2697 v4 @ 2.30GHz). The top, bottom, left and right boundary conditions are periodic and we are hence modelling the equivalent of an infinite number of slit apertures. Lastly, the space between the PG and the extraction grid (EG) is free of plasma (the gap is 3.5 mm and the width of the PG is 2 mm). The LHS of the simulation domain, PG, and EG are of Dirichlet type. The EG is biased at a voltage of 400V in the simulations while the other absorbing boundaries (PG and LHS) are set at 0V.

III. DESCRIPTION OF THE ELECTRONS MOTION ACROSS THE APERTURES

A. 2D versus 3D PIC-MCC calculation of a slit aperture of infinite length

In this section, we compare the plasma characteristics derived from a 2D versus 3D PIC-MCC model of a slit aperture of infinite length. The simulation domain for the 2D calculation is shown in fig. 2. We model the plane which includes the cusp field lines, i.e., the XZ plane of fig. 1. The particle drifts are out of the simulation domain and drift-wave type plasma instabilities are hence not described. The electrons which are extracted toward the accelerator diffuse across the field lines solely through collisions.

Next, we compare the 2D calculation to a 3D PIC-MCC model where the simulation domain is identical to the one of fig. 1 except that the slit aperture is of infinite length along (Oy); its width being 8 mm in the z-direction. Any occurrence of plasma instabilities in the plane perpendicular to the magnetic field lines, which could potentially increase the electron current transmitted across the aperture, will be modelled in this case. We found instead that the electron current collected on the extraction grid (EG) is identical in 2D and 3D, as shown in fig. 3. The latter plots the ratio (in percent) of the electron current impacting the EG divided by the total current flowing toward the PG inside the plasma volume. The level of numerical noise is logically higher in the 2D calculation due to the larger weight of the macroparticles. To further support the observation that the plasma properties are identical

in 2D and 3D in the case of slit apertures of infinite length, we show in fig. 4 the plasma potential profile along (Ox) for a location on the PG in the middle of the interstice between slit apertures. We compare the results from the 2D calculation versus estimates from the 3D PIC-MCC algorithm for either the case with two apertures or using a reduced domain in 3D where we modelled only one cusp, i.e., half the domain of fig. 1 along (Oz).

B. 3D PIC-MCC model of a slit aperture of finite length

We now analyse the electron kinetics for the case of a slit aperture of finite length. The simulation domain is described in details in sec. II and fig. 1. Figure 5 shows together the electron flux profiles in (i) the plane of the magnetic cusp field lines (XZ plane at $Y = 2.4$ cm), (ii) the plane where the electron drift occurs (XY plane at $Z = 0.6$ cm, crossing the middle of the slit aperture), (iii) the front of the PG and, lastly, (iv) the EG, respectively.

In (i), one can see the telltale sign of the electrons oscillating along the cusp field lines while in (ii), the electrons drift in the direction perpendicular to the magnetic field ($\mathbf{E} \times \mathbf{B}$ drift, see fig. 6 for an illustration using individual particle trajectories) and they can exit toward the accelerator only through one side of the slit aperture. Figure 6(a) shows one electron trajectory in the $Z = 0.6$ cm plane assuming that the Z component of its velocity is zero. When the electron reaches the edge of the plasma grid aperture, the electric field increases rapidly due to the large voltage of the extraction grid. This large non-uniformity of the electric field generates an electron drift across the magnetic field, i.e. the electron guiding center is no longer confined along an equipotential line as can be seen in fig. 6(a). This is a finite Larmor radius effect due to the electric field non uniformity (see for instance FF. Chen [20]).

In the case of fig. 6(a), the electron trajectory does not reach the extraction grid and ends up in the gap between the plasma grid and the extraction grid. The trajectories in fig. 6(b) and (c) are calculated in the 3D time averaged plasma potential. Electrons move both along the magnetic field lines, i.e, $v_z \neq 0$, and drift toward the right edge of the aperture. B_z decreases when the electron moves either upward in the direction of increasing Z or downward meanwhile the X component of the magnetic field, which is perpendicular to the EG, increases. The reason why the maximum electron current on the PG is seen on the two right corners of the aperture (see fig. 5) is therefore due to the combined effect of

the $\mathbf{E} \times \mathbf{B}$ drift and the electron motion along the magnetic field lines which spreads the drift current along (Oz) toward the corners of the aperture where B_z is weaker and where the electrons are more readily extracted to the EG. To illustrate our point, fig. 6(b) and (c) show three distinct categories of trajectories. (i) The electron is trapped and oscillates along the cusp magnetic field lines (blue color), collisions are necessary to un-trap the particle. (ii) The $\mathbf{E} \times \mathbf{B}$ drift directs the electron toward the PG where it impacts its surface (green color) and lastly, (iii) the electron drifts in the vicinity of the plasma meniscus and is extracted toward the EG (red color). Note that it may also drift some distance inside the accelerator before impacting the EG [9].

Comparing the case of a slit aperture of infinite (described in sec. III A) versus finite length, one observe than in the latter the electron current extracted toward the accelerator vessel is greatly enhanced by the $\mathbf{E} \times \mathbf{B}$ drift motion in front of the plasma meniscus. The ratio of the electron current impacting the EG divided by the total current flowing into the PG area (inside the plasma volume) is shown in fig. 7. We find that the current on the EG strongly varies versus time within a range for the transmission ratio between 50% and 100% (i.e., all the current). This is to be compared to the $\sim 22\%$ in the case of a slit aperture of infinite length. Such a large extracted current is induced by a plasma potentiel significantly higher than the average electron kinetic energy in the model as shown in fig. 4 (the temperature is $T_e = 2$ eV).

IV. UNSTABLE PLASMA BEHAVIOUR IN THE VICINITY OF THE PG

The large time variations of the current transmitted toward the EG in fig. 7 are due to strong fluctuations in the plasma quantities in the vicinity of the plasma meniscus. Figures 8 and 9 plots the electron flux and plasma potential profiles versus several time shots which are also displayed in fig. 7 for reference. The time window corresponds to approximatively two periods of oscillations. One can see that the flux profile is strongly modified, which is correlated with stiff changes of the plasma potential. We observe that (i) the electron flux follows approximately the potentiel lines in the aperture mid-plane plane as discussed previously in sec. III B (see also fig. 6), (ii) case A and I (D et G), which correspond to a maximum (minimum) transmission rate, share similar features, respectively. In D et G, the isopotential lines are twisted and we observe the appearance of potential wells (which attract

positively charged ions). The well forms due to a local increase of the electron density over a short time scale. The area of the well is accompanied by a double layer, i.e., over a short distance ($\sim \lambda_{De}$), the space charge ($n_e/n_i - 1$) switches from globally positive (excess of electrons) to negative. The direction of the electron flux is upward in fig. 8 and electrons experience a strong $\mathbf{E} \times \mathbf{B}$ drift in the vicinity of the aperture top edge in cases D et G (the 10V and 20V isopotential lines are very close in that area, hence the amplitude of the electric field is large, of order 20 kV/m for a magnetic field strength of 200G and a drift velocity $v_D \sim 10^6$ m/s, respectively). Such a situation is accompanied by a surge in transmission rate, as shown in fig. 7. In cases A and I, the electric field strength (and hence the drift velocity) is much lower in front of the aperture, which explains the drop in the electron current extracted toward the EG.

We can conclude that the current oscillations observed in the simulations are due to a drift instability induced by the charge separation associated with the electron loss to the extraction grid.

V. DISCUSSION

We modelled in this work a slit aperture of either finite or infinite length. We also performed simulations for cylindrical apertures and reached similar conclusions. In addition, for the case of negative ion sources for fusion applications, there is typically a large negative ion to electron ratio in the vicinity of the aperture. In Christ-Koch et al. for instance [21] the measured ratio n_-/n_e is about 0.4 in hydrogen and as high as 1.5 in deuterium 2 cm from the PG, inside the plasma volume. In these sources, the negative ions are produced on the surface of the PG as a byproduct of the impact of neutral hydrogen or deuterium atoms on the grid. The latter is covered by a thin layer of caesium to lower the work function of the metal increasing, as a consequence, the negative ions production yield. The adjunction of negative ions in our model did not modify the conclusions that an $\mathbf{E} \times \mathbf{B}$ drift near the plasma meniscus drives the electron current across the aperture toward the EG. The plasma density in the extraction region of these ion sources is typically sixty times larger than in our model, i.e., $n_i \simeq 3 \times 10^{17} \text{ m}^{-3}$, and hence the electron-ion Coulomb collision and the electron-neutral collision frequencies are of the same order of magnitude. The $\mathbf{E} \times \mathbf{B}$ drift remains the dominant electron extraction mechanism in our simulations when we artificially

increase ν_{ei} such that $\nu_{ei} \sim \nu_{en}$.

Lastly, in sec. IIIB, we found that a high fraction of the electron current flowing from the plasma volume toward the PG may be extracted (fig. 7). The extracted current can be significantly lowered in the model by biasing the PG with a voltage positive with respect to the ion source walls. In that case, the potential difference between the biased PG and the sheath potential is reduced and hence the electron current collected on the grid may be significantly increased. This technique is commonly employed in fusion-type ion sources used for Neutral Beam Injection (NBI) [18] .

VI. CONCLUSION

We analysed the transport of electrons across a grid with a slit aperture surrounded by a magnetic cups field profile. An electrode biased positively with respect to the grid is placed behind in order to produce an electric field which can extract negatively charged particles. In the case of negative ion sources, the role of the cusp field is to act as a barrier, preventing electrons from being extracted. The slit was either of finite or infinite length in the model. In the former, one found identical results between 3D and 2D PIC-MCC calculations indicating that the transport across the aperture is solely collisional. The plane which includes the cusp field lines was simulated in the 2D PIC-MCC model, hence any transport due to the magnetised drift dynamics was not included. In the 3D case, we found that the electron current transmitted onto the bias electrode (EG) was greatly enhanced compared to the 2D simulations. This is due to an $\mathbf{E} \times \mathbf{B}$ drift motion for the electrons where \mathbf{E} is the electric field of the plasma meniscus. The electrons escape parallel to one of the two edges of the slit aperture, being the only location where the drift velocity is directed toward the EG (the drift is generated by the B_z and E_y components in our configuration). Furthermore, we observed that the plasma parameters (potential, density, electron flux) are strongly fluctuating in front of the plasma meniscus resulting in a transmitted electron current ratio which varies within a factor of two over a time scale of $1 \mu s$. The maximum corresponds to an extraction of most of the electrons flowing onto the PG from the plasma volume in the conditions that we modelled. These oscillations are microinstabilities due to the charge separation induced by the loss of electrons to the extraction grid.

AUTHOR'S CONTRIBUTIONS

All authors contributed equally to this work.

ACKNOWLEDGMENTS

This work has been carried out within the framework of the EUROfusion Consortium and has received funding from the Euratom research and training programme 2014-2018 and 2019-2020 under grant agreement No 633053. The views and opinions expressed herein do not necessarily reflect those of the European Commission. Support from CEA and from the French Research Federation for Fusion Magnetic Confinement is also acknowledged.

AVAILABILITY OF DATA

The data that support the findings of this study are available from the corresponding author upon reasonable request.

-
- [1] E. Speth, H. Falter, P. Franzen, U. Fantz, M. Bandyopadhyay, S. Christ, A. Encheva, M. Früsche, D. Holtum, B. Heinemann, W. Kraus, A. Lorenz, C. Martens, P. McNeely, S. Obermayer, R. Riedl, R. Süss, A. Tanga, R. Wilhelm, and D. Wunderlich, *Nuclear Fusion* **46**, S220 (2006).
 - [2] P. McNeely, S. V. Dudin, S. Christ-Koch, U. Fantz, and the NNBI Team, *Plasma Sources Sci. Technol.* **18**, 014011 (2009).
 - [3] W. Kraus, D. Wunderlich, U. Fantz, B. Heinemann, F. Bonomo, and R. Riedl, *Review of Scientific Instruments* **89**, 052102 (2018).
 - [4] D. Wunderlich, R. Riedl, I. Mario, A. Mimo, U. Fantz, B. Heinemann, and W. Kraus, *Review of Scientific Instruments* **90**, 113304 (2019).
 - [5] M. Kashiwagi, N. Umeda, H. Tobari, A. Kojima, M. Yoshida, M. Taniguchi, M. Dairaku, T. Maejima, H. Yamanaka, K. Watanabe, T. Inoue, and M. Hanada, *Review of Scientific Instruments* **85**, 02B320 (2014).

- [6] K. Ikeda, H. Nakano, K. Tsumori, M. Kisaki, K. Nagaoka, M. Osakabe, Y. Takeiri, and O. Kaneko, *New Journal of Physics* **15**, 103026 (2013).
- [7] Y. Takao, K. Hiramoto, Y. Nakagawa, Y. Kasagi, H. Koizumi, and K. Komurasaki, *Japanese Journal of Applied Physics* **55**, 07LD09 (2016).
- [8] Y. Sato, H. Koizumi, M. Nakano, and Y. Takao, *Journal of Applied Physics* **126**, 243302 (2019).
- [9] G. Fubiani, H. P. L. de Esch, A. Simonin, and R. S. Hemsworth, *Phys. Rev. ST Accel. Beams* **11** (2008).
- [10] G. Fubiani, R. S. Hemsworth, H. P. L. de Esch, and L. Svensson, *Phys. Rev. ST Accel. Beams* **12**, 050102 (2009).
- [11] M. Cavenago, *AIP Conference Proceedings* **1869**, 020006 (2017).
- [12] G. Fubiani, L. Garrigues, G. Hagelaar, N. Kohen, and J. P. Boeuf, *New Journal of Physics* **19**, 015002 (2017).
- [13] W. L. Briggs, V. E. Henson, and S. F. McCormick, *A Multigrid Tutorial* (SIAM, 2000).
- [14] M. A. Lieberman and A. J. Lichtenberg, *Principles of Plasma Discharges and Materials Processing* (Wiley Interscience, 2005).
- [15] K. Nanbu, *Plasma Science, IEEE Transactions on* **28**, 971 (2000).
- [16] K. Nanbu, *Journal of the Physical Society of Japan* **49**, 2042 (1980).
- [17] V. Vahedi and M. Surendra, *Comp. Phys.Comm.* **87**, 179 (1995).
- [18] C. Wimmer and U. Fantz, *Journal of Applied Physics* **120**, 073301 (2016).
- [19] G. Fubiani and J. P. Boeuf, *Physics of Plasmas* **20**, 113511 (2013).
- [20] F. Chen, *Introduction to Plasma Physics and Controlled Fusion* (Springer, 1984).
- [21] S. Christ-Koch, U. Fantz, M. Berger, and N. Team, *Plasma Sources Science and Technology* **18**, 025003 (2009).
- [22] S. J. Buckman and A. V. Phelps, *The Journal of Chemical Physics* **82**, 4999 (1985).

TABLE I. Particle processes.

#	Reaction	Cross section ref.
1	$e + \text{H}_2 \rightarrow e + \text{H}_2$ (elastic)	[22]
2	$e + \text{H}_2^+ \rightarrow e + \text{H}_2^+$	[19]

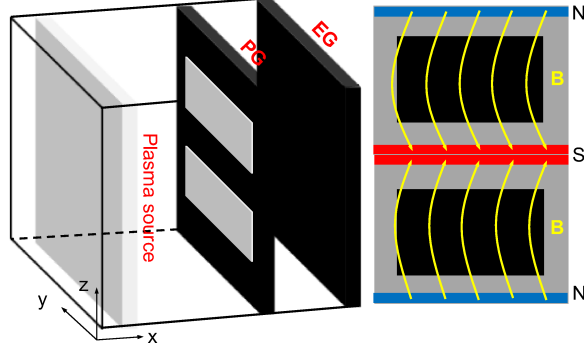


FIG. 1. Schematic illustration of the simulation domain. On the left-hand-side (LHS) is the plasma volume, which is separated from a biased electrode (EG) by a grid (PG) with two slit apertures (light grey). The volume between the PG and the EG is free of plasma. The latter is generated numerically by the injection of electron-positive ion pairs in the gray area labelled "plasma source". We fixed the plasma density in the model and hence each positive ion lost on a physical boundary (Dirichlet) is compensated by the re-injection of an electron-ion pair. The magnetic cusp field profile on the PG (in yellow) is shown in the right-hand-side (RHS) of the figure (the slit aperture is highlighted in black). In practice, this field would be generated by permanent magnet bars of reversed polarities (blue and red colours, N stands for "north" and S for "south"). The boundary condition on the LHS together with the plasma grid (PG) and extraction grid (EG) are of Dirichlet type while the top/bottom and left/right boundaries are periodic in 3D. The simulation box is $3.2 \times 4.8 \times 2.4 \text{ cm}^3$ (x, y, z) corresponding to a numerical resolution of $256 \times 384 \times 192$ grid nodes. The dimensions of the slit apertures are 4.3 cm along (Oy) and 0.8 cm in the z direction. The potential of the walls are 0V on the LHS plane $x = 0$ and PG (between $x = 2.65 \text{ cm}$ and $x = 2.85 \text{ cm}$) together with $V_{EG} = 400\text{V}$ (at $x = 3.2 \text{ cm}$), respectively.

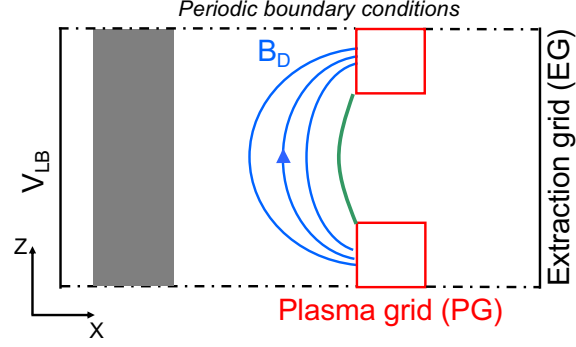


FIG. 2. Simulation domain for the 2D PIC-MCC calculation. The source term for the plasma is in the area highlighted in gray (where electron-positive ion pairs are injected). The field lines of the cusp magnetic field (\mathbf{B}_D) are drawn in blue. The slit aperture (in red) is of infinite length in 2D; its width is 8 mm. The simulation box is $3.2 \times 1.2 \text{ cm}^2$, the numerical resolution is 256×96 grid nodes, $V_{LB} = V_{PG} = 0\text{V}$, $V_{EG} = 400\text{V}$ and we implemented 40 particles per cells. The plasma meniscus is shown schematically in green.

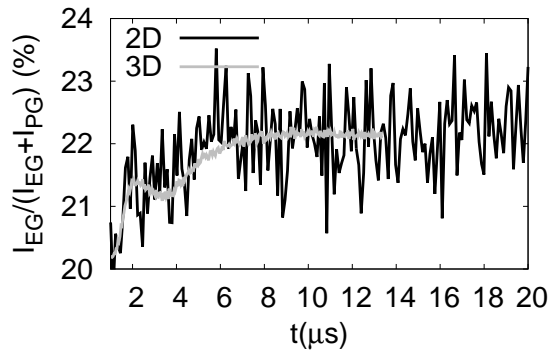


FIG. 3. Electron current collected on the extraction grid (EG). 2D versus 3D PIC-MCC calculation for a configuration with a slit aperture of infinite length.

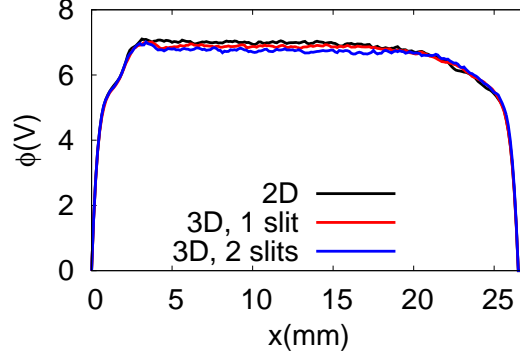


FIG. 4. Plasma potential profile along (Ox) for a position on the plasma grid (PG) corresponding to the middle of the interstice between two slit apertures. Estimates from the 2D PIC-MCC model (black solid line) are compared to the 3D PIC-MCC calculation for either a configuration with two slit apertures (blue solid line), as in fig. 1, or for half the simulation domain along (Oz), i.e., only one cusp (red solid line), respectively.

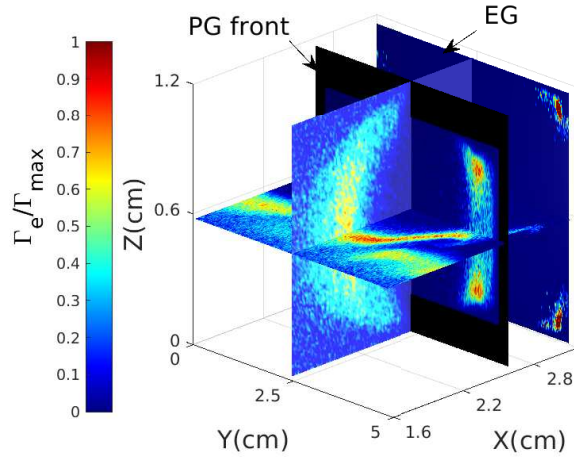


FIG. 5. 2D Electron flux profile. Four planes are displayed, that is, (i) the plane encompassing the cusp magnetic field line (XZ at $Y = 2.6$ cm), (ii) the electron $\mathbf{E} \times \mathbf{B}$ drift plane (XY, at $Z = 0.6$ cm, i.e., in the middle of the slit aperture), (iii) the front of the PG and, lastly, (iv) the EG, respectively. $\Gamma_{\max} = 3 \times 10^{21} \text{ m}^{-2} \cdot \text{s}^{-1}$.

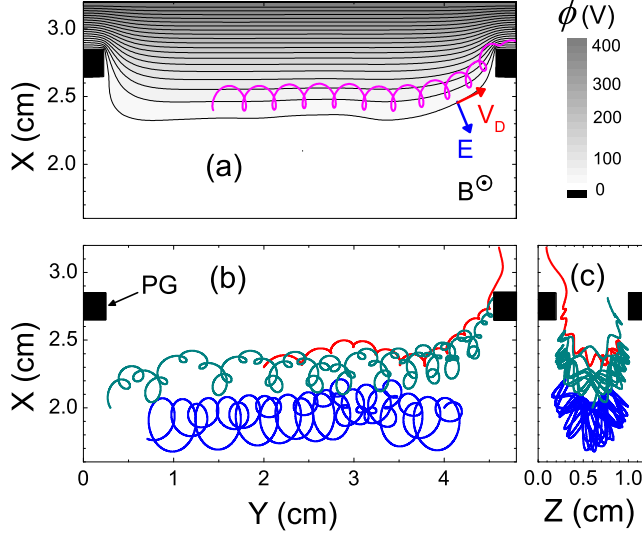


FIG. 6. Examples of electron trajectories, (a) in the $Z=0.6$ cm plane only (see fig. 5), (b) and (c) trajectories calculated in the 3D time averaged potential and projected on (a), the XY plane, and (b), the XZ plane, illustrating three typical cases. Blue trajectory: the trajectory is trapped and the electron oscillates back and forth in the cusp magnetic field. Collisions are needed to un-trap the electron and eventually move it to a green or red type of trajectories. Green trajectory: the electron undergoes $\mathbf{E} \times \mathbf{B}$ drift that draws it to the plasma grid. Red trajectory: the electron undergoes $\mathbf{E} \times \mathbf{B}$ drift. Due to the increasing X component of the electric field, and decreasing Z component of the magnetic field in the vicinity of the plasma grid (PG), the electron is no longer trapped by the magnetic field and can escape to the extraction grid (EG). The maximum current of extracted electrons is located in the top Y region of the PG due to $\mathbf{E} \times \mathbf{B}$ drift (direction shown in (a)) and in the top and bottom Z corners of the PG because the Z component of the magnetic field decreases in these cusp regions. The initial conditions (index 0) of the four trajectories are as follows. Purple trajectory: initial positions $x_0 = 1.5$ cm, $y_0 = 2.4$ cm, initial kinetic energy $E_0 = 2$ eV, initial components of the velocities $v_{x0} = \sqrt{eE_0/m_e}$ and $v_{y0} = -v_{x0}$, respectively. Blue trajectory: $x_0 = 2$ cm, $y_0 = 4$ cm, $z_0 = 0.6$ cm, kinetic energy (in eV) $E_0 = m_e/2ev_0^2 = 3$ eV, velocities $v_{x0} = v_{y0} = v_{z0} = v_0\sqrt{3}$. Green trajectory: $x_0 = 2$ cm, $y_0 = 0.3$ cm, $z_0 = 0.6$ cm, $E_0 = 2$ eV, $v_{x0} = -v_{y0} = v_0\sqrt{0.4}$, $v_{z0} = v_0\sqrt{0.2}$. Red trajectory: $x_0 = 2.3$ cm, $y_0 = 2$ cm, $z_0 = 0.7$ cm, $E_0 = 2$ eV, $v_{x0} = v_{y0} = v_0\sqrt{2}$, $v_{z0} = 0$. The isopotential contours (black solid lines) are displayed in (a) together with the amplitude of the potential (grey scale).

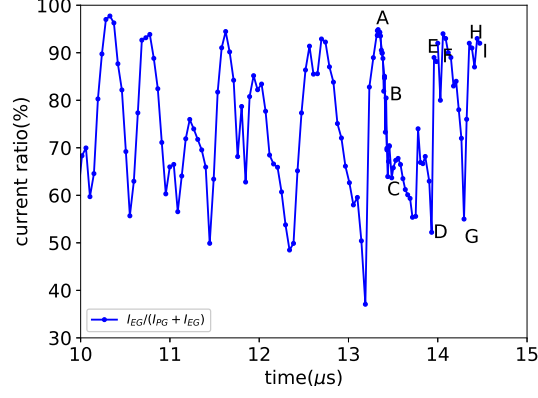


FIG. 7. Ratio of the electron current collected on the EG divided by the total current flowing toward the PG, $I_{EG}/(I_{EG} + I_{PG})$ (in percent) versus time. I_{EG} (I_{PG}) is the current impacting the EG (PG), respectively.

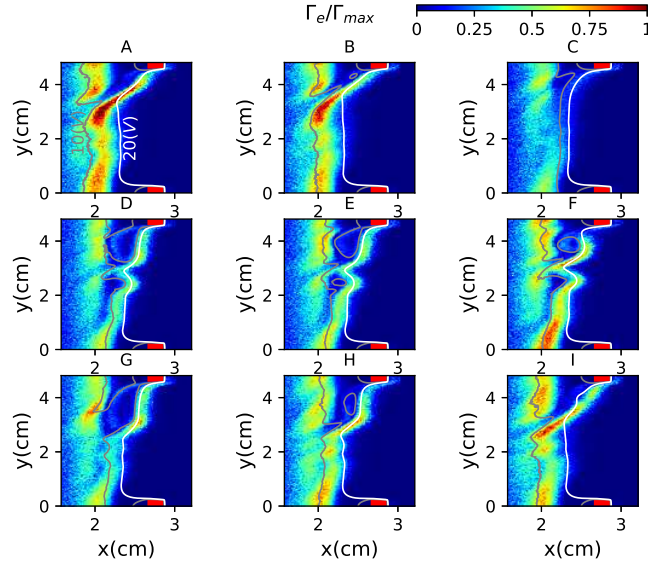


FIG. 8. Electron flux profile in the plane $Z = 0.6$ cm of fig. 5 for different time shots labeled from A to I (which are also indicated in fig. 7 for reference). The isopotential lines for $\phi = 10$ V and 20V inside the plasma volume are also shown. $\Gamma_{\max} = 2.3 \times 10^{21} \text{ m}^{-2} \cdot \text{s}^{-1}$.

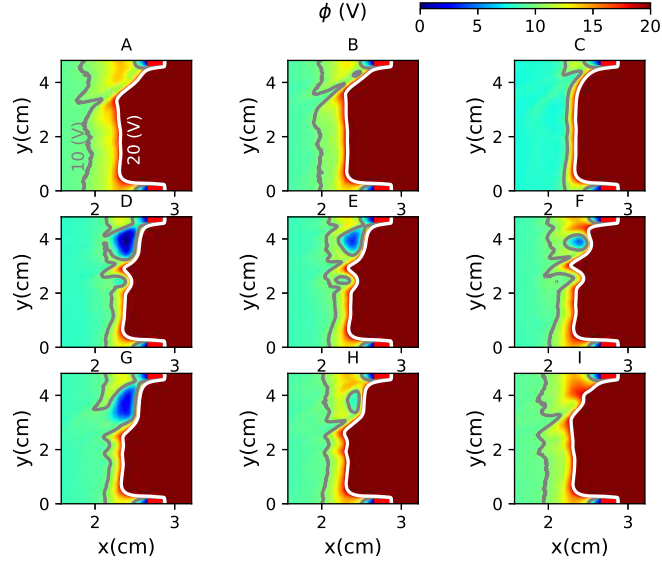


FIG. 9. Plasma potential profile in the slit aperture mid-plane ($Z = 0.6$ cm) for different time shots.